RESEARCH ARTICLE

Multi-Physics Characteristics of PMSM for Compressor According to Driving Mode Considering PWM Frequency

CHI-SUNG PARK[1], **JAE-HYUN KIM**[1], (Graduate Student Member, IEEE),
SOO-HWAN PARK[1,2], **YOUNG-DOO YOON**[1], (Senior Member, IEEE),
AND MYUNG-SEOP LIM[1], (Member, IEEE)
[1]Department of Automotive Engineering, Hanyang University, Seoul 04763, South Korea
[2]Research and Development Division, Hyundai Motor Company, Hwaseong 18280, South Korea

Corresponding author: Myung-Seop Lim (myungseop@hanyang.ac.kr)

ABSTRACT When pulse width modulation (PWM) technique is used for permanent magnet synchronous motors (PMSMs) for compressors, current harmonics in the carrier frequency domain are inevitably generated. These current harmonics not only affect losses in PMSM and drive, but also create harmonic components of the electromagnetic force, which causes noise/vibration. Since the amplitude and harmonic order of the current harmonics depend on the driving mode, the efficiency and noise are also affected by the driving mode. Therefore, this paper presents the comparison of the efficiency, noise, and vibration characteristics of compressor PMSM according to the driving mode. In particular, space vector PWM (SVPWM), discontinuous PWM (DPWM), and square-wave modes were analyzed. First, the characteristics of the experimental current waveform for each driving mode are analyzed, and the time and spatial orders of the electromagnetic force are calculated based on the Maxwell stress tensor method. Then, based on the derived electromagnetic force, the noise/vibration characteristics of PMSM are analyzed. The efficiencies of PMSM, driving, and total (PMSM+drive) were compared according to driving mode. It was confirmed that there is a trade-off relationship between efficiency and noise/vibration according to the driving modes. All results were analyzed using finite element analysis and experimentally verified using manufactured motor.

INDEX TERMS Carrier frequency, compressor, efficiency, electromagnetic force density, noise and vibration, permanent magnet synchronous motor (PMSM), pulse width modulation (PWM).

I. INTRODUCTION

Recently, energy efficiency has gained interest-in most industries with the strengthening of energy efficiency regulations. The rating standards of home appliances are being raised by introducing energy efficiency classes. For refrigerators, the efficiency and noise/vibration characteristics are important because these appliances consume a large amount of power and are located indoors [1]. The compressor, which is the component of the refrigerator that compresses and circulates the refrigerant to produce the cold air necessary for the refrigerator, has the greatest impact on its efficiency and

The associate editor coordinating the review of this manuscript and approving it for publication was Jinquan Xu.

noise/vibration [2]. In the past, the compressors for refrigerators mainly consisted of an induction motor for constant speed or inverter-motor system for variable-speed operation. Recently, due to increasing efficiency concerns, inverter-motor systems using PMSM have become mainstream [3], [4], [5]. Among the various types of PMSM, interior permanent magnet synchronous motors (IPMSM), which are advantageous in terms of high-power density and efficiency, are preferred. IPMSMs are classified as integer slot distributed windings and fractional slot concentrated windings (FSCW), and the type is determined by the pole slot combination [6]. The FSCW is mainly used in refrigerator compressors owing to its high manufacturability compared to integer slot windings. It generates many electromagnetic force spatial
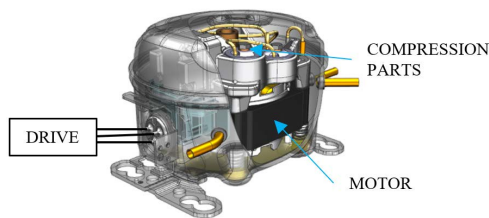
FIGURE 1. Structure of the compressor used in the refrigerator.

harmonics by the armature magnetomotive force (MMF) and slot effect and has a lower vibration order compared to integer slot windings [7], [8], [9]. Therefore, studies to improve the vibration characteristics of FSCW PMSM are being actively conducted because their noise/vibration characteristics are degraded compared to that of integer slot windings [10], [11], [12], [13].

Fig. 1 shows the structure of the compressor used in the refrigerator. The compressor system comprises three main parts: motor, drive, and compression, which affect the efficiency of the compressor system. In particular, the driving mode is closely related to multi-physics characteristics such as the efficiency and noise/vibration of the motor [14], [15], [16], [17], [18], [19], [20], [21].

In general, the driving modes used for compressor motors include SVPWM, DPWM, and square-wave mode. During each cycle of the carrier frequency, the SVPWM, DPWM, and square-wave mode are turned on/off six times, four times, and once, respectively. Thus, the switching loss of the inverter according to the driving mode is large in the following order: SVPWM, DPWM, and square-wave mode. However, as the number of on/off switching decreases, the ripple of the armature current increases, which affects the electromagnetic loss of the motor. Therefore, the electromagnetic loss according to the driving mode is large in the following order: square-wave mode, DPWM, and SVPWM.

Also, the PWM harmonics of the armature current generate MMF harmonics in the stator. This is an important part of the electromagnetic radial force that causes electromagnetic noise and vibrations. Therefore, the driving mode should be selected by considering the total efficiency and noise/vibration of the motor and drive. In this study, the efficiency of the motor drive system and noise/vibration characteristics according to the driving mode, considering the PWM current, were analyzed.

II. NOISE AND VIBRATION OF PMSM BY DRIVING MODE

In this section, the electromagnetic force density and noise/vibration of the motor considering the PWM frequency are compared after analyzing the input current for each driving mode. Here, the commercial software JMAG program was used for two-dimensional (2D) and three-dimensional (3D) electromagnetic finite element analysis (FEA).
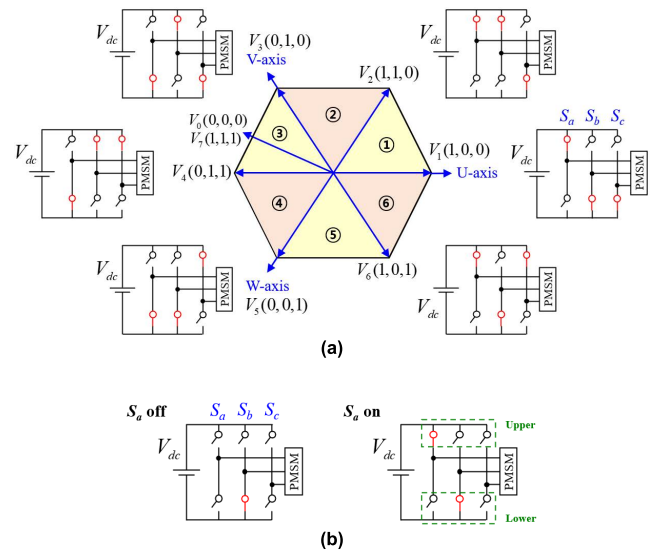

FIGURE 2. Voltage vector diagrams and switching states. (a) SVPWM and DPWM. (b) Square wave.

A. ANALYSIS OF THE PWM CURRENT

Fig. 2(a) shows the voltage vector diagram and the states of the switching elements. SVPWM and DPWM have a total of 8 different switching states in a 3-phase inverter. The voltage vectors V_1-V_6 are effective-voltage vectors for applying a voltage to the PMSM. V_0 and V_7 are zero-voltage vectors because no valid voltage can be applied to the PMSM. Fig. 2(b) shows the switching state of the square wave mode. When the S_b lower element is kept on, and the S_a upper element is turned on/off, AC power is supplied to phase U and armature current flows alternately.

Fig. 3 shows the switching method according to the driving modes and the measured current waveform, where f_c is the carrier frequency. As the current ripple-induced electromagnetic force is influenced by the carrier frequency, f_c is set to 4.5 kHz in order to compare the multi-physics characteristics of PMSM according to the driving mode. In SVPWM, all three-phase switching elements are on/off within the cycle of the carrier frequency. The zero-voltage vector is located on both sides (V_0) and at the center (V_7) within the cycle of the carrier frequency. Therefore, the frequency of the main current ripple is twice to the carrier frequency, and the amplitude of current ripple is smaller than other driving mode. In DPWM mode, the frequency of main current ripple is same as the carrier frequency because there is no zero-voltage vector in the center of the cycle of the carrier frequency. For this reason, DPWM has a large current ripple compared to SVPWM. In square wave mode, two switching devices operates simultaneously for 120° commutation with constant duty ratio. Therefore, the frequency of the main current ripple is the same as the carrier frequency.

Fig. 4 shows the comparison of harmonic currents for each driving mode through the fast Fourier transform (FFT) analysis. The total harmonic distortion (THD) of the armature current is large in the order of square wave, DPWM, and
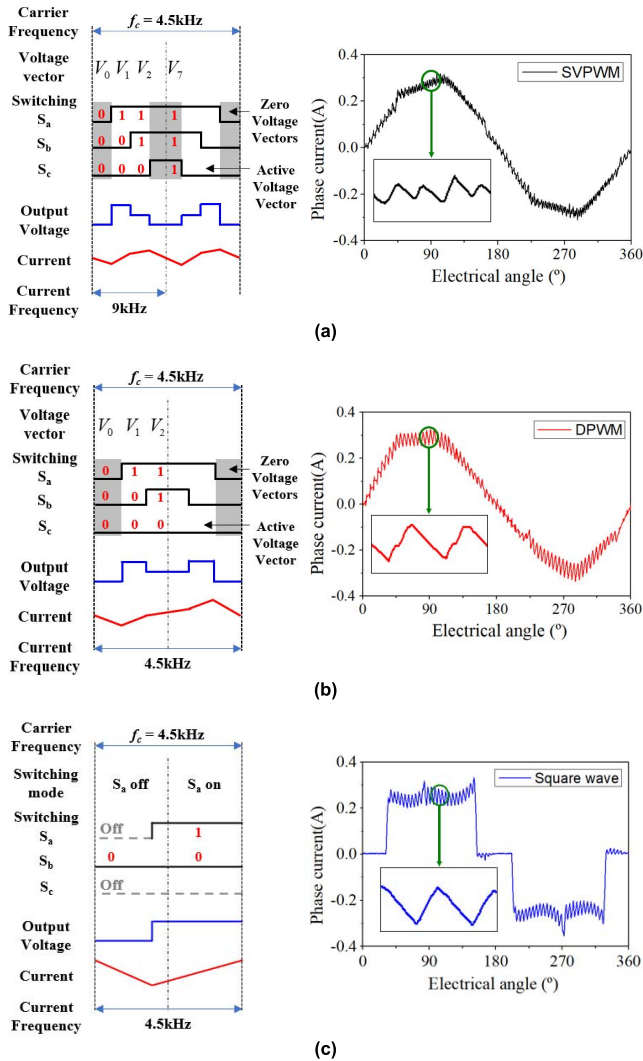
FIGURE 3. Switching method and waveform of the measured current. (a) SVPWM. (b) DPWM. (c) Square wave.

FIGURE 4. Harmonics analysis of the waveform of the measured current. (a) SVPWM. (b) DPWM. (c) Square wave.
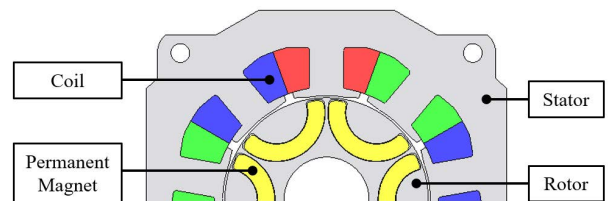
FIGURE 5. Configuration of the motor.

TABLE 1. Specification of the IPMSM.

Quantity	Unit	Value
Number of poles / slots	-	6 / 9
PM remanence	T	0.45
Airgap length	mm	0.6
Stack length	mm	26
Rated torque	Nm	0.21
Speed range	Hz	20 ~75

SVPWM. In SVPWM, the main frequency of current ripple is 9 kHz, which is twice to the carrier frequency. On the other hand, the main frequency of current ripple for DPWM and square wave drive is 4.5 kHz, which is equivalent to the carrier frequency. The square-wave mode has a small fundamental magnitude owing to the characteristics of the current waveform, and the harmonics are larger than those of other driving modes in the region below 4 kHz. In the carrier frequency domain, the harmonics of the input current appear large at the same frequency as the cycle of the current determined by the driving mode.

B. ELECTROMAGNETIC FORCE DENSITY BY DRIVING MODE

In this section, we compare the electromagnetic force densities in the radial and tangential directions of the motor for each driving mode. The configuration of the motor is shown in Fig. 5 and the specifications of the IPMSM are summarized in Table 1.
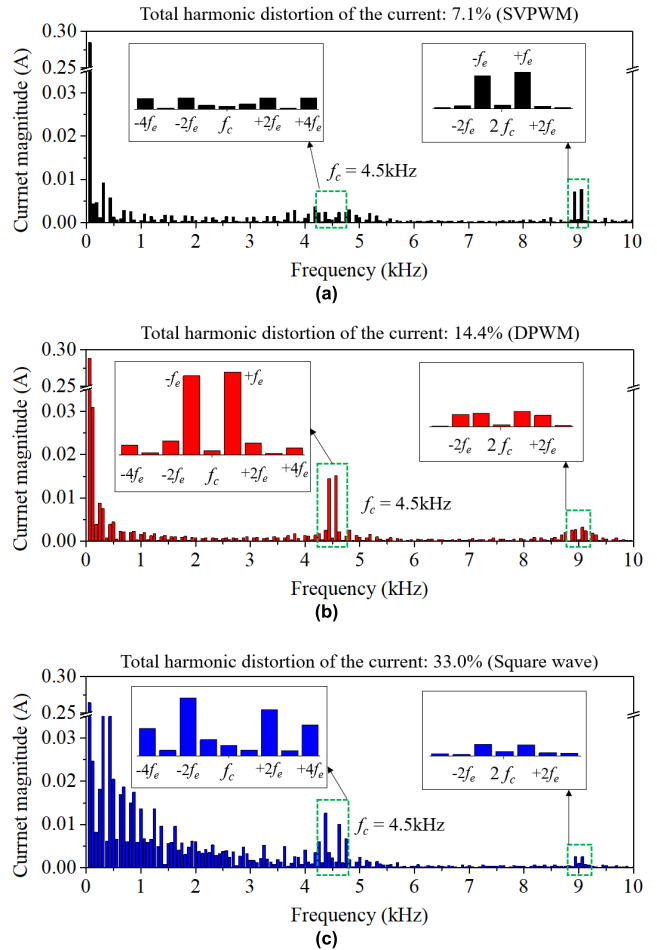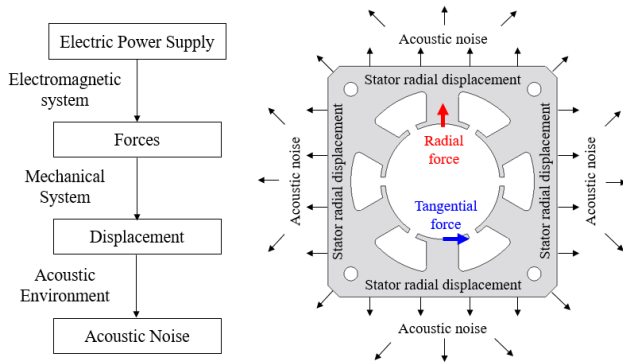
FIGURE 6. Mechanism for the generation of vibration and noise in electrical machines.

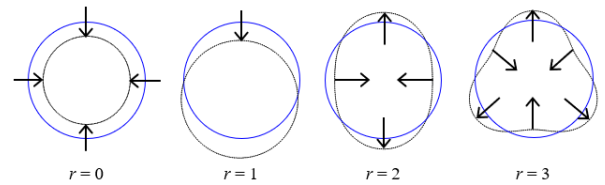| Sources	Vibration order	Frequency
PM field	$p(\mu_1\pm\mu_2)$	$f_e(\mu_1\pm\mu_2)$
Interaction of the PM field and stator slotting	$p(\mu_1\pm\mu_2)\pm ks$	$f_e(\mu_1\pm\mu_2)$
Armature reaction	$p(v_1\pm v_2)$	$f_e(n_1\pm n_2)$
Interaction of the armature reaction and stator slotting	$p(v_1\pm v_2)\pm ks$	$f_e(n_1\pm n_2)$
Interaction of the PM field and armature reaction	$p(\mu\pm v)$	$f_e(\mu\pm n)$
Interaction of the PM field, armature reaction, and stator slotting	$p(\mu\pm v)\pm ks$	$f_e(\mu\pm n)$

FIGURE 7. Stator deformation due to radial forces with vibration order of 0, 1, 2, and 3.

Noise and vibrations in the motor are caused by the generation of electromagnetic forces. When electric power is supplied to the motor, a magnetomotive force is applied to the air gap, which can be expressed as the magnetic flux density of the air gap. The Maxwell stress tensor method is used to calculate the electromagnetic force from the magnetic flux density in the air gap. The electromagnetic force is excited to the stator and vibrations are generated in the motor. In addition, the generated vibration causes motor noise. Fig. 6 shows the mechanism of noise/vibration of the motor.

The magnetomotive force is divided into the permanent magnet (PM) field magnetomotive force and armature magnetomotive force, which can be expressed as [13] and [19].

$$F_{PM} = \sum_{\mu=2k\pm1} F_\mu \cos(\mu p\omega t - \mu p\alpha + \theta_\mu) \quad (1)$$

$$F_{armature} = \sum_n \sum_v F_v \cos(np\omega t - vp\alpha) \quad (2)$$

Here, μ, p, ω, t, α, θ, n, and v represent the spatial harmonic order of the PM field, pole pair, electrical angular velocity, time, mechanical angle, phase angle, time harmonic order of the armature reaction, and spatial harmonic order of the armature reaction, respectively.

The magnetic flux density in the air gap can be expressed as the sum of the armature magnetomotive force and the PM field magnetomotive force, and the product of relative permeance is shown below [12], [17].

$$B = \Lambda_g(F_{PM} + F_{armature}) \quad (3)$$

Here, Λ_g is the relative permeance of the air gap which can be expressed as follows [13], [19].

$$\Lambda_g = \frac{\mu_0}{g}\left(1 + \sum_k A_k \cos(ks\alpha)\right) \quad (4)$$

Here, μ_0 is the vacuum permeability, g is the air gap length, A_k is the harmonic permeance, s is the slot number, and k is an integer. The spatial harmonic order of the armature reaction v can be determined by the pole–slot combination as follows [13].

$$q = \frac{s}{2mp} = \frac{z}{c}, \quad v = \frac{2mk}{c} + 1 \quad (5)$$

Here, q and m are the slot number per phase per pole and number of phases, respectively, while c and z are relatively prime. Using the Maxwell stress tensor method, the radial electromagnetic force density can be expressed as the radial and tangential magnetic flux densities in the air gap, as follows [13], [17].

$$P_r = \frac{B_r^2 - B_t^2}{2\mu_0} \approx \frac{B_r^2}{2\mu_0} \quad (6)$$

Here, B_r and B_t are the radial and tangential air gap flux densities, respectively. B_r and B_t neglect the slot effects. In general, because B_r is much larger than B_t, the radial electromagnetic force density can be approximated using only B_r. The radial electromagnetic force density P_r can be derived using (1)-(6). Thus, the radial electromagnetic force expressed as combinations of the PM field, armature reaction, and slot effect, constituting the magnetic flux density in the air gap.

The vibration orders and frequencies of the radial electromagnetic force for various source combinations are summarized in Table 2. The radial electromagnetic force is a function of time and spatial, and the vibration order, which is the spatial order of the radial force, has a great influence on the vibration deformation of the stator. Fig. 7 shows the stator deformation associated with the vibration order r of the radial force. The amplitude of the stator deformation for vibration order $r = 0$ and vibration order $r \geq 2$ can be expressed

TABLE 3. Vibration orders of the 6-pole 9-slot PMSM at twice the fundamental.

Sources	Vibration order	Frequency
PM field	6 (=2p)	$2f_e$
Interaction of the PM field and stator slotting	$6\pm9k$	$2f_e$
Armature reaction	$6\pm9k$	$2f_e$
Interaction of the armature reaction and stator slotting	$6\pm9k$	$2f_e$
Interaction of the PM field and armature reaction	$6\pm9k$	$2f_e$
Interaction of the PM field, armature reaction, and stator slotting	$6\pm9k$	$2f_e$

as (7), (8), respectively [23].

$$D_{r=0} = \frac{R_y R \cdot FM_{r=0}}{E \cdot T_y} \qquad (7)$$

$$D_{r\geq2} = \frac{12R_y^3 R \cdot FM_{r\geq2}}{E \cdot T_y^3 (r^2-1)^2} \qquad (8)$$

where R_y is the yoke average radius, R is the inner radius of the stator, T_y is the yoke radial thickness, E is the Young's modulus, FM is the magnitude of the force, and $FM_r = 0$ denotes the amplitude of the zeroth-order electromagnetic force, $FM_{r\geq2}$ is the amplitude of the harmonics of the radial electromagnetic force of order r. When the vibration order $r \geq 2$, the amount of deformation of the stator is almost inversely proportional to the fourth power of the vibration order r. Since the same motor is used in this paper, the structural dimensions, physical properties, and vibration order are the same. Therefore, the difference in harmonic amplitude according to the driving mode is expressed as the difference in vibration/noise of the motor.

In general, the electromagnetic force is generated by the synthesis of the fundamental air-gap magnetic flux density and possesses the largest amplitude at $2f_e$, which is twice the fundamental frequency. Therefore, the vibration order of the 6-poles and 9-slots motor used in this study was calculated at $2f_e$, as shown in Table 3. The vibration order generated by the PM field is the 6th order, which is twice that of the pole pair. All sources except the PM field occurred at the orders of $6 \pm 9k$ at $2f_e$. Therefore, the 6-pole 9-slot PMSM has vibration orders of $\ldots, -30, -21, -12, -3, 6, 15, 24, \ldots$ at $2f_e$. A 2D electromagnetic FEA with the PWM current shown in Fig. 3 was conducted to derive an accurate radial electromagnetic force density. The load condition, electrical angular velocity, and carrier frequency were 0.21 Nm, 60 Hz, and 4.5 kHz, respectively. So, the harmonic orders for f_c and $2f_c$ were the 75th and 150th, respectively.

Fig. 8 shows the results of the 2D FFT on the radial electromagnetic force density according to the driving mode. The 6th order, which was the PM field source, and the $6 \pm 9k$ orders, which were other sources, displayed a large amplitude at $2f_e$(= 120 Hz). At $2f_e$, which corresponds to

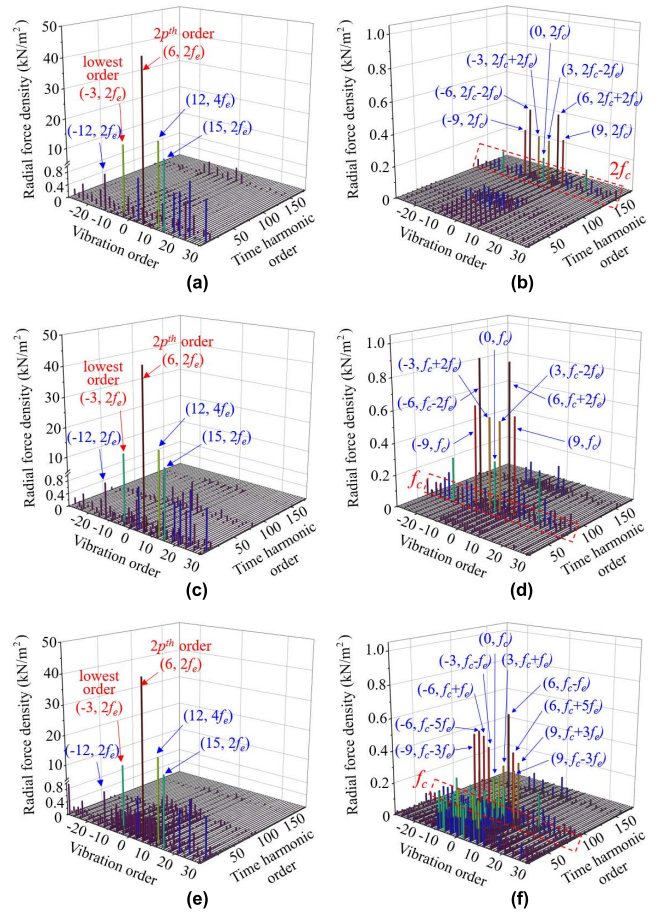**FIGURE 8.** Radial electromagnetic force density according to the driving mode: (a) SVPWM. (b) f_c band of SVPWM. (c) DPWM. (d) f_c band of DPWM. (e) Square wave. (f) f_c band of square wave.

the largest radial electromagnetic force density, the vibration orders for the driving modes are the same and exhibit similar amplitudes. However, according to the characteristics of the current waveform analyzed above, the radial electromagnetic force density of the square-wave driving mode is widely distributed in the region below f_c owing to current harmonics. Comparing the carrier frequency band, the current harmonics and electromagnetic forces are both large in the $2f_c$ region, in the SVPWM driving mode. The DPWM and square wave driving modes also exhibit a large electromagnetic force density at f_c where the current harmonics are large. This is equal to the frequency cycle of the current waveform.

Table 4 lists the harmonic frequencies of the current waveform for each driving mode. The carrier frequency sideband harmonic component of the input current generates the armature air gap magnetic flux density harmonic. The generated armature harmonics react with the PM field fundamental component to generate electromagnetic force density harmonics. Table 5 shows the time and vibration orders of the radial electromagnetic force density for each driving mode in the carrier frequency domain.

Local tangential forces should also be considered when analyzing vibrations. When a local tangential force is applied

TABLE 4. Frequency of the PWM harmonic of the input current.

Frequency	SVPWM	DPWM	Square wave
f_c	$f_c \pm 2f_e$	$f_c \pm f_e$	$f_c \pm 2f_e, f_c \pm 4f_e$
$2f_c$	$2f_c \pm f_e$	$2f_c \pm f_e, 2f_c \pm 2f_e$	$2f_c \pm f_e$

TABLE 5. Frequency and vibration order of PWM related.

Frequency	Vibration order	SVPWM	DPWM	Square wave
f_c	$-6(=-2p) \pm 9k$	$f_c + f_e$	$f_c - 2f_e$	$f_c - 5f_e, f_c + f_e$
	$0 \pm 9k$	$f_c \pm 3f_e$	f_c	$f_c \pm 3f_e$
	$6(=2p) \pm 9k$	$f_c - f_e$	$f_c + 2f_e$	$f_c - f_e, f_c + 5f_e$
$2f_c$	$-6(=-2p) \pm 9k$	$2f_c - 2f_e$	$2f_c - 2f_e, 2f_c + f_e$	$2f_c - 2f_e$
	$0 \pm 9k$	$2f_c$	$2f_c$	$2f_c$
	$6(=2p) \pm 9k$	$2f_c + 2f_e$	$2f_c - f_e, 2f_c + 2f_e$	$2f_c + 2f_e$

TABLE 6. Maximum values of the electromagnetic force density for each driving mode in the carrier frequency domain (Vibration order $r = 0$).

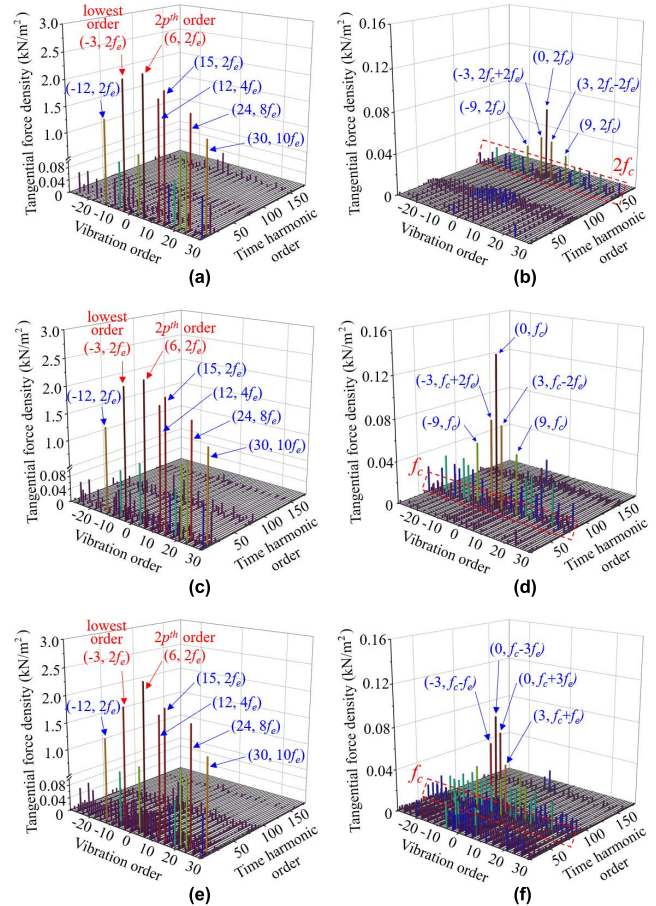| Direction	Frequency, Unit	SVPWM	DPWM	Square wave
Radial	f_c, kN/m^2	0.018	0.319	0.265
	$2f_c$, kN/m^2	0.159	0.061	0.030
Tangential	f_c, kN/m^2	0.012	0.142	0.094
	$2f_c$, kN/m^2	0.071	0.028	0.023

TABLE 7. Maximum values of the electromagnetic force density for each driving mode in the carrier frequency domain (Vibration order $r = 3$).

Direction	Frequency, Unit	SVPWM	DPWM	Square wave
Radial	f_c, kN/m^2	0.055	0.577	0.441
	$2f_c$, kN/m^2	0.288	0.118	0.099
Tangential	f_c, kN/m^2	0.009	0.082	0.068
	$2f_c$, kN/m^2	0.041	0.017	0.014

FIGURE 9. Tangential electromagnetic force density according to the driving mode: (a) SVPWM. (b) f_c band of SVPWM. (c) DPWM. (d) f_c band of DPWM. (e) Square wave. (f) f_c band of square wave.

to the tooth edge and causes a lever arm effect, it generates radial vibration in the same direction as the radial force [22]. The tangential electromagnetic force density is expressed by the Maxwell stress tensor method as the radial and tangential air-gap flux densities, as follows.

$$P_t = \frac{B_r B_t}{\mu_0} \quad (9)$$

2D electromagnetic FEA was also performed for the tangential electromagnetic force density under the same conditions as in the radial direction. A 2D FFT was performed on the tangential electromagnetic force density according to the driving mode, and the results are shown in Fig. 9. Comparing with the radial electromagnetic force density, the amplitude of the tangential force density is observed to be small. However, the magnitude of the 6$^{\text{th}}$ vibration order ($= 2P$) by the PM field of the tangential electromagnetic force density is similar to that of other electromagnetic force densities. Thus, when the armature harmonics and PM field fundamentals react to produce an electromagnetic force density, the $2P$ component

of the tangential vibration order does not occur significantly in the carrier frequency band.

Table 6 and 7 list the maximum values of radial and tangential electromagnetic force densities for each driving mode in the carrier frequency domain at vibration orders $r = 0$ and $r = 3$, respectively. The electromagnetic force of the 1$^{\text{st}}$ and 2$^{\text{nd}}$ of the vibration order r does not occur, and in the conditional vibration order $r \geq 2$ in equation (8), the lowest order is $r = 3$. The maximum values of the electromagnetic force density are the results of the 2D electromagnetic FEA shown in Fig. 8, 9. SVPWM has the lowest electromagnetic force density in the radial/tangential direction and vibration orders $r = 0$ and $r = 3$. And the generated electromagnetic force in the radial direction is much greater than that in the tangential direction. In the next section, the vibration characteristics of the motor are analyzed according to the electromagnetic force density for each driving mode.

C. NOISE AND VIBRATION
The relationship between the electromagnetic force density and vibration was analyzed by performing a vibration test and 3D FEA analysis for each driving mode. Fig. 10 shows
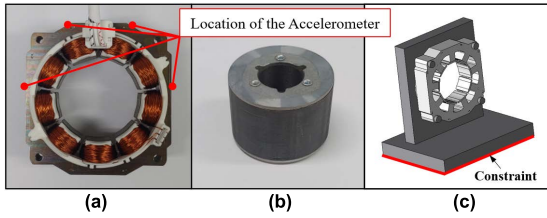
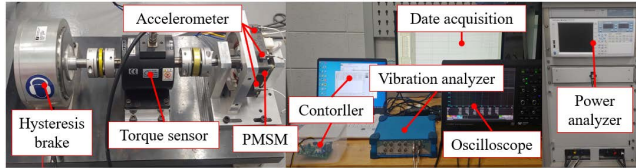**FIGURE 10.** Prototypes and 3D model. (a) Stator. (b) Rotor. (c) 3D structural model.

FIGURE 11. Setup for the vibration and efficiency test.

FIGURE 12. Vibration test and 3D FEA results for the various driving modes at the rated load condition. (a) SVPWM. (b) DPWM. (c) Square wave.

the manufactured stator and rotor for the test and structural model for the 3D FEA analysis. For the structural model, constraints were applied to the L-jig floor in the same manner as the vibration tests. Fig. 10(a) shows the mounting positions of the four accelerometers. Four accelerometers were mounted to the PMSM surface, two of which were mounted to the teeth of the stator and the rest were mounted to the yokes on either side of the stator. The accelerometer was of type 8776A50 from Kistler, and adhesive was used for mounting. The vibration test environment, which is shown in Fig. 11, includes a hysteresis brake, torque sensor, PMSM, accelerometer, controller, data acquisition system, vibration analyzer, oscilloscope, and power analyzer. The vibration test was performed under the rated load condition, electrical angular velocity of 60 Hz, and torque of 0.21 Nm.

Fig. 12 shows a comparison of the 3D FEA results analyzed using the measured PWM currents with the experimental results. The test and simulation results are similar, and the vibration displacement and electromagnetic force density exhibit high values at the same frequency. DPWM and SVPWM had the largest displacements in the f_c and $2f_c$ regions, respectively. This is consistent with the harmonic characteristics obtained via FFT analysis of the input current for each driving mode. The main electromagnetic force density in the carrier frequency domain is generated by the synthesis of the armature harmonic and fundamental PM field. Because the same PMSM is used, the electromagnetic force density and vibration change according to the characteristics of the armature harmonics for each driving mode.

Vibration on the surface of the motor generates noise, and the acoustic power radiated through the vibration velocity of the surface can be predicted. The acoustic power generated in a unit surface area can be expressed approximately as follows [24].

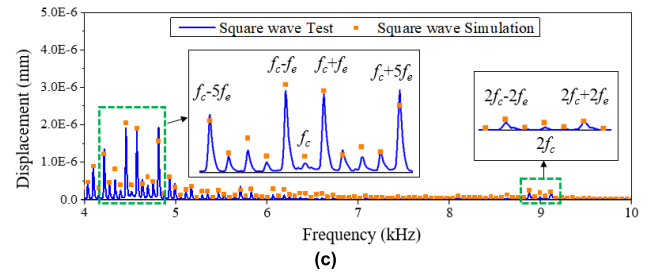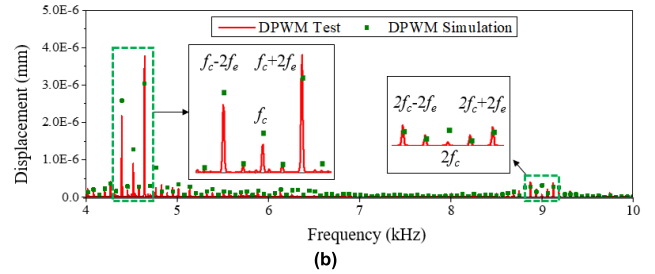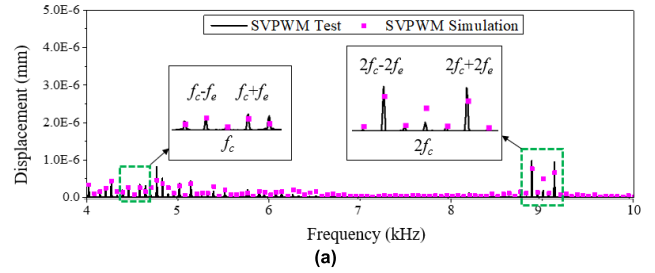$$P_{acousticpower} = \frac{1}{2}\rho_0 c_0 v^2 dS\sigma \qquad (10)$$

Here, ρ_0 is the density of the medium, c_0 is the speed sound, v is the average of vibration velocity, dS is the unit surface area, and σ is radiation efficiency. Assuming that the motor is driven in the same environment, the noise increases as the vibration velocity of the motor surface increases. From the vibration test results of PMSM, it can be expected that DPWM has the highest noise in the f_c region, and SVPWM has the highest noise in the $2f_c$ region.

Fig. 13 shows the 3D FEA results of noise for each driving mode. The result corresponds to the same electrical angular velocity (60 Hz) and torque (0.21 Nm) as the vibration analysis conditions. Here, air was used as the medium around the motor. The carrier frequency domain exhibits the same trend as the results of the electromagnetic force density and vibration analyses. In the region below the carrier frequency (60 Hz - 4 kHz), the noise of the square-wave driving mode is high. Because shown in Fig. 4, 8, and 9, the square wave mode has a wider and larger electromagnetic force density than the other driving modes in the region below the carrier frequency. Therefore, the overall noise according to the driving mode is large in the following order: square wave mode, DPWM, and SVPWM. The 3D FEA analysis of the noise was performed from 60 Hz to 12 kHz with a cycle of an electrical angular velocity of 60 Hz, and the overall noise was calculated
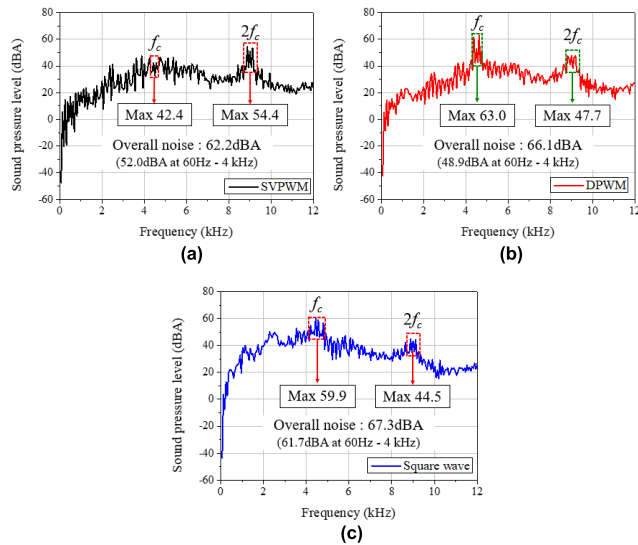
FIGURE 13. 3D FEA results of noise for the various driving modes. (a) SVPWM. (b) DPWM. (c) Square wave.

FIGURE 14. Comparison of noise and vibration factors by driving mode. (a) f_c. (b) $2f_c$.

as follows.

$$Overall\,noise = 10\log(10^{L_1/10} + 10^{L_2/10} + \cdots + 10^{L_n/10}) \quad (11)$$

Here, L_1 is the value of the sound pressure level at 60 Hz, and L_2 is the value of the sound pressure level at 120 Hz. The overall noise used in this paper is the sum of sound pressure levels. Fig. 14 compares the factors related to noise and vibration for each driving mode. If the magnitude of the current harmonic is large, the electromagnetic force density and vibration displacement are also large, and they are also connected to noise. Therefore, the driving mode and carrier frequency must be selected appropriately. This is because the characteristics of the current harmonics are different depending on the driving mode and carrier frequency.

III. EFFICIENCY OF PMSM FOR VARIOUS DRIVING MODES

In this section, the efficiency and loss of the motors and drives for various driving modes are compared. The operating range of the PMSM compressor used in this study is 20-75 Hz. After stabilizing the refrigerator temperature, the main operating range was 20-30 Hz, and the load condition was 0.21 Nm. Therefore, the performance tests were conducted at 20, 25, and 30 Hz. Here, the JMAG was used for 2D FEA analysis.

A. EFFECT OF PWM CURRENT FOR COPPER AND IRON LOSS

The motor loss is divided into copper loss, which occurs when current flows through the copper wire, and iron loss, which occurs when magnetic flux is linked to the iron core. The motor losses were derived by conducting 2D FEA with the PWM current shown in Fig. 3.
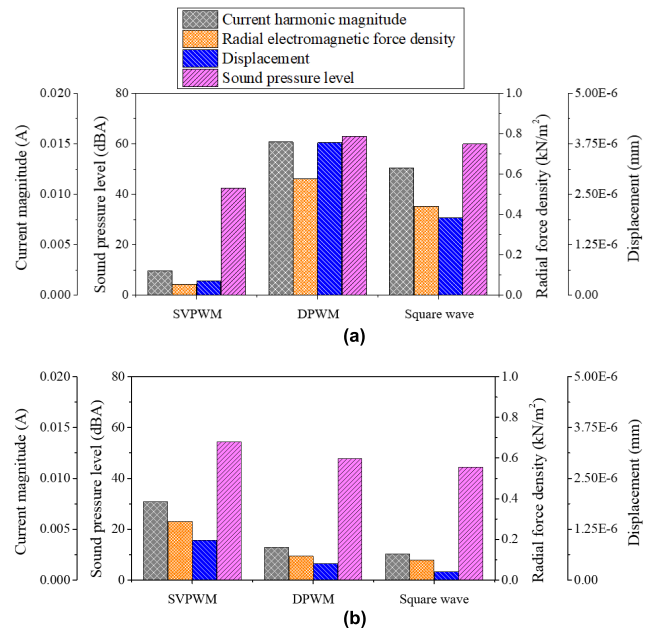
The copper loss is calculated as the sum of the losses owing to the fundamental and harmonics, as follows.

$$P_{copper\ losses} = P_1 + \sum_e P_e \quad (12)$$

Here, P_1 and P_e represent the copper loss owing to the fundamental and harmonics, respectively, where e is the order of the harmonic. The iron loss, which is proportional to the magnetic flux density and frequency, is expressed as follows [6].

$$P_{iron\ losses} = k_h B^n f + k_e B^2 f^2 + k_a B^{1.5} f^{1.5} \quad (13)$$

Here, B, f, k_h, k_e, and k_a represent the magnetic flux density, frequency, hysteresis loss factor, eddy-current loss factor, and anomalous loss factor, respectively.

Fig. 15 shows the results of the motor loss analysis using 2D FEA. Both the copper and iron losses in the motor are the smallest with SVPWM. The fundamental component exhibits similar losses according to the driving mode, but the harmonic losses are different. The harmonic ratio of the loss according to the driving mode is large in the following order: square-wave mode, DPWM, and SVPWM. This is equivalent to the order of the harmonic ratios of the input current. In addition, since the iron loss is proportional to the frequency, the harmonic ratio is larger than that of the copper loss. Hence, a lower harmonic ratio of the input current corresponds to a lower motor loss. Table 8 shows the harmonic ratio of loss for various driving modes.
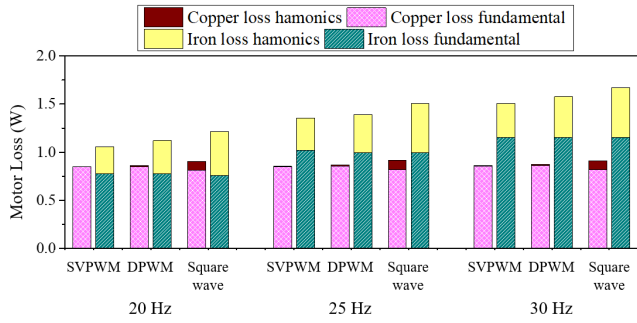
FIGURE 15. Comparison of losses owing to the fundamental and harmonics of the motor.

TABLE 8. Harmonic ratio of copper loss and iron loss for various driving modes.

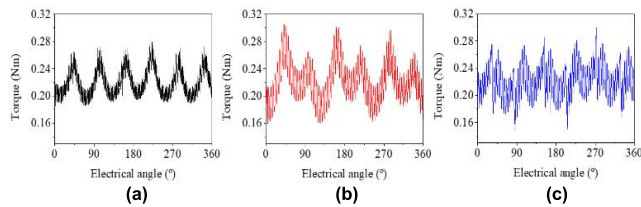| Driving mode	Loss	Harmonic ratio (%)		
		20 Hz	25 Hz	30 Hz
SVPWM	Copper / Iron	0.5 / 26.6	0.6 / 24.5	0.6 / 23.5
DPWM		1.6 / 31.0	1.4 / 28.3	1.5 / 26.8
Square wave		10.3 / 37.4	10.1 / 33.6	10.0 / 31.2

FIGURE 16. Torque ripple for each driving mode for one cycle of the electrical angle. (a) SVPWM (b) DPWM (c) Square wave.

Fig. 16 shows the torque ripple for each driving mode. The torque of a 3-phase motor can be approximated as follows.

$$T = \frac{1}{\omega_m}\sum_{m=1}^{3}\sum_{h}\sum_{j}\left\{\begin{array}{l} I_h E_j \cos\left[h\left(\omega_e t - \frac{2\pi m}{3}\right)\right] \\ \times \cos\left[j\left(\omega_e t - \frac{2\pi m}{3}\right)\right]\end{array}\right\} \quad (14)$$

Here, ω_m is mechanical angular velocity, m is phase number (U, V, W = 1, 2, 3), h is time harmonic order of the current, j is time harmonic order of the back- electromotive force (BEMF), I is magnitude of current, E is magnitude of BEMF, ω_e is electrical angular velocity, t is time.

Therefore, the input current affects the torque ripple of the motor because the BEMF and the current are combined to generate the torque. As for the current frequency cycle, SVPWM is 9 kHz, DPWM and square wave mode are 4.5 kHz. As shown in Fig. 4, since SVPWM has the smallest harmonic magnitude of the current frequency, the harmonic ripple of the torque is also the smallest. In DPWM, the reason the torque ripple has a 3rd order component is because the 2nd harmonic of the current is large. In square wave mode, the harmonics of the current are widely distributed, so that there are torque harmonics of various orders. Torque ripple can create shaft speed oscillation, which can increase noise/vibration in the belt/gear system. Therefore, it can be
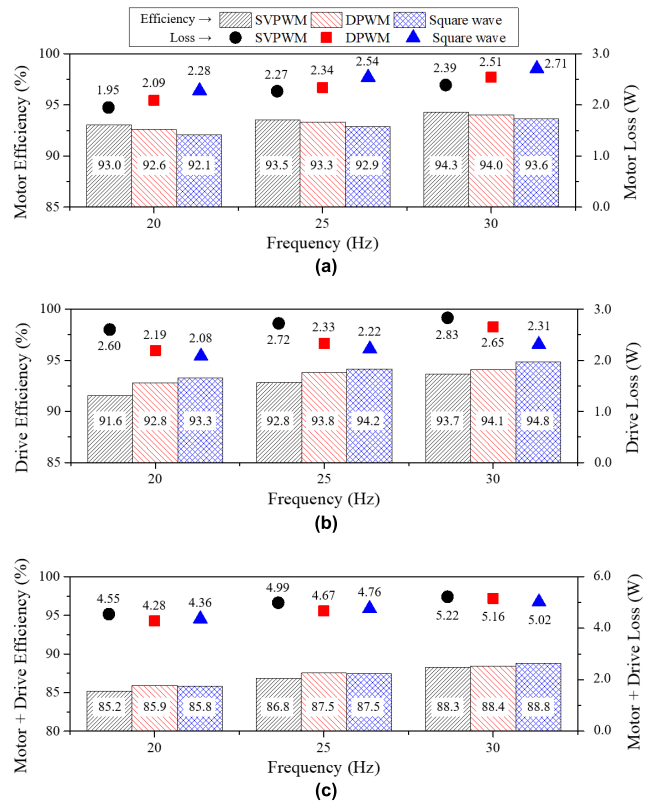

FIGURE 17. Results of efficiency test according to the driving mode. (a) Motor. (b) Drive (c) Motor + Drive.

predicted that SVPWM produces the smallest noise/vibration even in the belt/gear system compared to other driving modes. The eddy current loss occurring in the permanent magnet was excluded from the analysis because this motor uses a ferrite magnet whose permanent magnet eddy current loss is very small within the main operating frequency.

B. VERIFICATION OF THE EFFICIENCY OF PMSM BY DRIVING MODE
The motor performance test was set up in the same configuration as that of the vibration test. Fig. 17 shows the results of the efficiency and loss tests according to the driving mode. The SVPWM and square-wave mode exhibit the highest motor and driving efficiencies, respectively. The total efficiency of the motor and drive is high for the DPWM and square-wave mode. The motor losses are large in the following order: square-wave mode, DPWM, and SVPWM. The drive loss includes the switching and conduction losses of six switching devices of the 3-phase and the losses of the other PCB components. The drive losses in SVPWM, which switches six times during one cycle of the carrier frequency, are the highest. Total loss, including the motor and drive, is the highest in SVPWM at 20–30 Hz. Fig. 18 shows the results of the comparison of the motor losses. The copper and iron losses of the motor according to the driving mode are similar to those of the 2D FEA results.
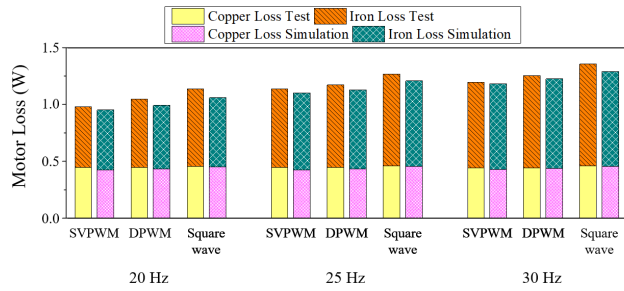
FIGURE 18. Comparison of the motor loss obtained using 2D FEA and test results.

TABLE 9. Efficiency and NVH characteristics by driving mode under refrigerator compressor conditions.

| Driving mode | Efficiency | | | Noise |
	Motor	Drive	Total	Vibration
SVPWM	◎	△	○	◎
DPWM	○	○	◎	○
Square wave	△	◎	◎	○

Summarizing together with the noise and vibration characteristics analyzed previously, under the refrigerator compressor condition, SVPWM is advantageous in terms of noise and vibration, and DPWM/square wave mode is advantageous in terms of performance. Table 9 shows the efficiency and noise/vibration characteristics according to the driving mode. Also, depending on the driving mode and carrier frequency, the frequency range where noise and vibration occur is different, and the loss of the motor changes. Therefore, it is good to appropriately select the driving mode and carrier frequency in consideration of these characteristics. For example, the refrigerator compressor PMSM sets an arbitrary carrier frequency by avoiding the resonance frequency of the compressor and refrigerator. Usually, an arbitrary carrier frequency is determined above 2 kHz. As the loss of the motor depends on the load on the refrigerator, the selected carrier frequency is changed up and down to find the highest total efficiency point and the lowest noise/vibration point.

IV. CONCLUSION

This study compared the efficiency of three driving modes (SVPWM, DPWM, and square wave) used in refrigerator compressors, and compared the noise and vibration in the carrier frequency domain. First, comparing the input current, the THD of the input current was 7.1%, 14.4%, and 33.0% in SVPWM, DPWM, and square wave modes, respectively. The harmonic components of the input current create electromagnetic force density and cause noise/vibration in the motor. Therefore, the overall noise of the motor was lower in the order of SVPWM (62.2dBA), DPWM (66.1dBA), and square wave mode (67.3dBA). In the carrier frequency domain, since the current harmonic of the DPWM was the largest, the noise and vibration of the motor was also the largest. Also, because the harmonics of the input current cause harmonic losses of

copper and iron, the motor efficiency, which is the average from 20 Hz to 30 Hz, was highest at 93.6% in SVPWM and lowest at 92.9% in square wave mode. In drive efficiency, the SVPWM had the largest loss because it performed the most switching on/off, and the square wave motor with the smallest number of switching had the lowest loss. The average total efficiency between 20 Hz and 30 Hz was similar for DPWM and square wave mode at 87.3% and 87.4%, respectively, and SVPWM was the lowest at 86.8%.

REFERENCES

[1] J. Y. Jeon, J. You, and H. Y. Chang, "Sound radiation and sound quality characteristics of refrigerator noise in real living environments," *Appl. Acoust.*, vol. 68, no. 10, pp. 1118–1134, Oct. 2007.

[2] J. Guo, J. Luo, Y. Guo, X. Pan, X. Fang, and X. Wu, "Noise test and control for household refrigerator compressor," in *Proc. IEEE Int. Conf. Inf. Autom.*, Aug. 2015, pp. 112–115.

[3] X. Liu, H. Chen, J. Zhao, and A. Belahcen, "Research on the performances and parameters of interior PMSM used for electric vehicles," *IEEE Trans. Ind. Electron.*, vol. 63, no. 6, pp. 3533–3545, Jun. 2016.

[4] P. H. Nguyen, E. Hoang, and M. Gabsi, "Performance synthesis of permanent-magnet synchronous machines during the driving cycle of a hybrid electric vehicle," *IEEE Trans. Veh. Technol.*, vol. 60, no. 5, pp. 1991–1998, Jun. 2011.

[5] K. T. Chau, C. C. Chan, and C. Liu, "Overview of permanent-magnet brushless drives for electric and hybrid electric vehicles," *IEEE Trans. Ind. Electron.*, vol. 55, no. 6, pp. 2246–2257, Jun. 2008.

[6] C. Zhou, X. Huang, Z. Li, and W. Cao, "Design consideration of fractional slot concentrated winding interior permanent magnet synchronous motor for EV and HEV applications," *IEEE Access*, vol. 9, pp. 64116–64126, 2021.

[7] A. M. El-Refaie, "Fractional-slot concentrated-windings synchronous permanent magnet machines: Opportunities and challenges," *IEEE Trans. Ind. Electron.*, vol. 57, no. 1, pp. 107–121, Jan. 2010.

[8] Z. Wu, Y. Fan, C. H. T. Lee, D. Gao, and K. Yu, "Vibration optimization of FSCW-IPM motor based on iron-core modification for electric vehicles," *IEEE Trans. Veh. Technol.*, vol. 69, no. 12, pp. 14834–14845, Dec. 2020.

[9] T. Sun, J.-M. Kim, G.-H. Lee, J.-P. Hong, and M.-R. Choi, "Effect of pole and slot combination on noise and vibration in permanent magnet synchronous motor," *IEEE Trans. Magn.*, vol. 47, no. 5, pp. 1038–1041, May 2011.

[10] Z. Wu, Y. Fan, H. Wen, and D. Gao, "Vibration suppression of FSCW IPM with auxiliary slots," in *Proc. IEEE Energy Convers. Congr. Expo.*, Sep. 2018, pp. 3222–3227.

[11] F. Lin, S.-G. Zuo, W.-Z. Deng, and S.-L. Wu, "Reduction of vibration and acoustic noise in permanent magnet synchronous motor by optimizing magnetic forces," *J. Sound Vibrat.*, vol. 429, pp. 193–205, Sep. 2018.

[12] S. Zuo, F. Lin, and X. Wu, "Noise analysis, calculation, and reduction of external rotor permanent-magnet synchronous motor," *IEEE Trans. Ind. Elect.*, vol. 62, no. 10, pp. 6204–6212, Oct. 2015.

[13] D.-Y. Kim, M.-P. Park, J.-H. Sim, and J.-P. Hong, "Advanced method of selecting number of poles and slots for low-frequency vibration reduction of traction motor for elevator," *IEEE/ASME Trans. Mechatronics*, vol. 22, no. 4, pp. 1554–1562, Aug. 2017.

[14] K.-W. Lee, S. Park, and S. Jeong, "A seamless transition control of sensorless PMSM compressor drives for improving efficiency based on a dual-mode operation," *IEEE Trans. Power Electron.*, vol. 30, no. 3, pp. 1446–1456, Mar. 2015.

[15] L. Chang, W. Lee, T. Jahns, and J. Kim, "Comparative analysis of PWM power losses in IPM machines with different modulation schemes using wide-bandgap-based inverters," in *Proc. IEEE Energy Convers. Congr. Exposit. (ECCE)*, Oct. 2020, pp. 3629–3636.

[16] R. M. Pindoriya, B. S. Rajpurohit, and R. Kumar, "A novel application of harmonics spread spectrum technique for acoustic noise and vibration reduction of PMSM drive," *IEEE Access*, vol. 8, pp. 103273–103284, 2020.

[17] T. Hara, T. Ajima, K. Hoshino, and A. Ashida, "Carrier electromagnetic vibration of DC voltage fluctuation in permanent-magnet synchronous motor with distributed winding," *IEEE Trans. Ind. Appl.*, vol. 56, no. 5, pp. 4623–4631, Sep. 2020.

[18] J. Xu and H. Zhang, "Random asymmetric carrier PWM method for PMSM vibration reduction," *IEEE Access*, vol. 8, pp. 109411–109420, 2020.

[19] F. Lin, S. Zuo, W. Deng, and S. Wu, "Modeling and analysis of electromagnetic force, vibration, and noise in permanent-magnet synchronous motor considering current harmonics," *IEEE Trans. Ind. Electron.*, vol. 63, no. 12, pp. 7455–7466, Dec. 2016.

[20] S.-H. Park, J.-C. Park, S.-W. Hwang, J.-H. Kim, H.-J. Park, and M.-S. Lim, "Suppression of torque ripple caused by misalignment of the gearbox by using harmonic current injection method," *IEEE/ASME Trans. Mechatronics*, vol. 25, no. 4, pp. 1990–1999, Aug. 2020.

[21] E. K. Kim, W. Song, Y. S. Kwon, J. H. Kim, H. M. Yoon, H. G. Lee, and J. Y. Yoon, "Vibration-generation mechanism and reduction method in linear iron-cored permanent-magnet synchronous motors at stationary state," *IEEE/ASME Trans. Mechatronics*, vol. 27, no. 5, pp. 3397–3406, Jan. 2022.

[22] H. Lan, J. Zou, Y. Xu, and M. Liu, "Effect of local tangential force on vibration performance in fractional-slot concentrated winding permanent magnet synchronous machines," *IEEE Trans. Energy Convers.*, vol. 34, no. 2, pp. 1082–1093, Jun. 2019.

[23] S. Wang, J. Hong, Y. Sun, and H. Cao, "Analysis of zeroth-mode slot frequency vibration of integer slot permanent-magnet synchronous motors," *IEEE Trans. Ind. Electron.*, vol. 67, no. 4, pp. 2954–2964, Apr. 2020.

[24] L. E. Kinsler, A. R. Frey, A. B. Coppens, and J. V. Sanders, *Fundamentals of Acoustics*, 4th ed. New York, NY, USA: Wiley, 2000.

CHI-SUNG PARK received the master's degree in electrical engineering from Pusan National University, Pusan, South Korea, in 2011. He is currently pursuing the Ph.D. degree in automotive engineering with Hanyang University, Seoul, South Korea.

Since 2010, he has been with LG Electronics, Changwon, South Korea, where he is currently a Senior Research Engineer. His research interests include the design, and the analysis of vibration and noise of electric machines.

JAE-HYUN KIM (Graduate Student Member, IEEE) received the bachelor's degree in mechanical engineering from Hanyang University, Seoul, South Korea, in 2017, where he is currently pursuing the Ph.D. degree in automotive engineering.

His research interests include the design, and the analysis of vibration and noise of electric machines.

SOO-HWAN PARK received the bachelor's degree in mechanical engineering and the Ph.D. degree in automotive engineering from Hanyang University, Seoul, Republic of Korea, in 2014 and 2022, respectively.

From 2019 to 2020, he was with the Korea Institute of Industrial Technology, Republic of Korea. Since 2022, he has been with the Research and Development Division of Hyundai Motor Company, Republic of Korea, where he is currently a Senior Research Engineer. His research interests include electromagnetic field analysis, design, and optimization of electric machines for automotive and robotics applications, and thermal management system for electric vehicles.

YOUNG-DOO YOON (Senior Member, IEEE) was born in South Korea. He received the B.S., M.S., and Ph.D. degrees in electrical engineering from Seoul National University, Seoul, South Korea, in 2002, 2005, and 2010, respectively. From 2010 to 2013, he was at Samsung Electronics Company, South Korea, as a Senior Engineer. From 2013 to 2017, he was an Assistant Professor with the Department of Electrical Engineering, Myongji University, Yongin, South Korea. Since 2017, he has been an Assistant Professor with the Department of Automotive Engineering, Hanyang University, Seoul. His current research interests include power electronic control of electric machines, high power converter, and electric home appliances.

MYUNG-SEOP LIM (Member, IEEE) received the bachelor's degree in mechanical engineering and the master's and Ph.D. degrees in automotive engineering from Hanyang University, Seoul, South Korea, in 2012, 2014, and 2017, respectively.

From 2017 to 2018, he was a Research Engineer at Hyundai Mobis, Yongin, South Korea. From 2018 to 2019, he was an Assistant Professor with Yeungnam University, Daegu, South Korea, Since 2019, he has been with Hanyang University, where he is currently an Assistant Professor. His research interests include electromagnetic field analysis and electric machinery for mechatronics systems, such as automotive and robot applications.

• • •